PHYSICAL REVIEW B **97**, 064425 (2018)

Magnetic phase diagram of $Sr_{2-x}La_xIrO_4$ synthesized by mechanical alloying

K. Horigane,[1] M. Fujii,[2] H. Okabe,[3] K. Kobayashi,[1,2] R. Horie,[1] H. Ishii,[4] Y. F. Liao,[4] Y. Kubozono,[1] A. Koda,[3]
R. Kadono,[3] and J. Akimitsu[1]
[1]*Research Institute for Interdisciplinary Science, Okayama University, Okayama, Japan*
[2]*Graduate School of Natural Science and Technology, Okayama University, Okayama, Japan*
[3]*Institute of Materials Structure Science/J-PARC Center, KEK, Ibaraki, Japan*
[4]*National Synchrotron Radiation Research Center, Hsinchu 30076, Taiwan*

(Received 10 October 2017; revised manuscript received 23 January 2018; published 28 February 2018)

We report the crystal structure and physical properties of $Sr_{2-x}La_xIrO_4$ synthesized by mechanical alloying. The magnetic transition temperature T_N and electrical resistivity decreased with increasing La doping, consistent with previous studies involving single-crystalline samples. We also identified the relationship between T_N and tetragonal distortion (c/a) in this system. This result suggests that the magnetism of the Sr214 system is strongly correlated with its crystal structure. Zero-field muon spin rotation/relaxation studies revealed that short-range antiferromagnetic ordering is realized in $Sr_{1.9}La_{0.1}IrO_4$; also, the spin-glass state is stabilized in the low-temperature region. The Ir moment estimated from the longitudinal field μSR results is 0.045 μ_B, ten times smaller than that of Sr_2IrO_4 ($\sim$0.4 μ_B), indicating that electrons are introduced into the Ir atoms.

DOI: 10.1103/PhysRevB.97.064425

I. INTRODUCTION

Due to their wide variety of physical properties, such as charge and spin ordering, colossal magnetoresistance, and high-T_c superconductivity, 3d transition-metal oxides (TMOs) have attracted much attention. These physical properties emerge from the interplay between the spin, charge, and orbital degrees of freedom. In contrast, 5d TMOs should exhibit exotic phenomena because their spin-orbit coupling (SOC) is one order of magnitude larger than that of 3d TMOs. Recently, Kim *et al.* proposed a spin-orbit Mott state with a local $J_{\rm eff} = 1/2$ wave function produced by the interplay between SOC and Coulomb U in Sr_2IrO_4 [1]. In this insulator, which effectively contains one electron per Ir ion, the pseudospin remains a good quantum number and orders antiferromagnetically. Resonant inelastic x-ray scattering (RIXS) revealed that the magnon dispersion in Sr_2IrO_4 is well described by the antiferromagnetic (AF) Heisenberg model with a superexchange interaction of $J_{\rm eff} = 1/2$ moments on a square lattice [2]. More recently, our group performed angle-resolved photoelectron spectroscopy (ARPES) measurements of electron-doped $Sr_{2-x}La_xIrO_4$ ($x =$ 0, 0.04, 0.08), and observed a dispersive in-gap state that evolves with carrier doping [3]. This in-gap state was also observed in hole-doped $La_{2-x}Sr_xCuO_4$ [4] and electron-doped $Nd_{2-x}Ce_xCuO_4$ [5]. Due to the similar Mott physics between cuprates and iridates, Sr_2IrO_4 is a good candidate for exploring unconventional high-T_c superconductivity by carrier doping.

Watanabe *et al.* theoretically predicted that electron-doped Sr_2IrO_4 exhibits d-wave superconductivity formed by the $J_{\rm eff} = 1/2$ Kramers doublet [6]. Instead, a triplet p-wave superconducting state was found on the hole-doping side [7]. The physical properties of electron-doped Sr_2IrO_4 systems have been extensively studied in experiments by several groups. Castaneda *et al.* reported the structure and magnetic properties of polycrystalline samples of $Sr_{2-x}La_xIrO_4$. They found that the electrical resistivity increases with increasing La concentration, and their magnetic susceptibility results revealed canted antiferromagnetism below 240 K in both Sr_2IrO_4 and electron-doped $Sr_{1.85}La_{0.15}IrO_4$ [8]. However, in neuron scattering and magnetic susceptibility measurements using single-crystalline samples of $Sr_{2-x}La_xIrO_4$, the long-range AF order was suppressed up to $x = 0.08$ and the short-range AF order persisted up to $x = 0.12$ with La doping [9]. Qi *et al.* reported that introducing oxygen vacancies into single-crystal $Sr_2IrO_{4-\delta}$ ($0 < \delta < 0.04$) significantly decreased the resistivity; also, $Sr_2IrO_{4-\delta}$ ($\delta = 0.04$) underwent a metal-insulator transition at 105 K [10]. Thus the differences in the physical properties of polycrystal and single-crystal $Sr_{2-x}La_xIrO_4$ remain an unresolved issue.

In previous studies of polycrystalline $Sr_{2-x}La_xIrO_4$ samples, the powder samples were synthesized by a short heating and quenching technique. Therefore, in this study, we synthesized our samples using mechanical alloying (MA), which is well known to improve chemical reactions. We report the crystal structure and physical properties of $Sr_{2-x}La_xIrO_4$ derived from synchrotron powder x-ray diffraction, magnetic susceptibility, electrical resistivity, and muon-spin relaxation (μSR) measurements.

II. EXPERIMENTAL PROCEDURE

Polycrystalline samples of $Sr_{2-x}La_xIrO_4$ were prepared by conventional solid-state reactions. A mixture of $SrCO_3$ ($0 < x < 0.1$), SrO ($0.11 < x < 0.2$), La_2O_3, and IrO_2 was ground and further mixed by planetary ball milling (Fritsch, P-7) at a rotation rate of 400 rpm for 3 h with 15 (5 mm-diameter) and 10 (10 mm-diameter) ZrO_2 balls. The resulting powders were calcined in air at 1150 °C for 15 min.

Magnetic susceptibility measurements were performed using a superconducting quantum interference device magnetometer (Quantum Design MPMS-R2). The electrical resistivity was measured by a conventional dc four-probe method with a measuring current I of 1 mA in the temperature range 2–300 K. Scanning electron microscope (SEM) images were recorded using a field emission SEM (FE-SEM) ULTRA55 scanning electron microscope at 10 kV.

X-ray diffraction studies were performed using a conventional x-ray spectrometer with a graphite monochromator (RINT-1100, Rigaku). Synchrotron powder XRD experiments were conducted using the BL12B2 beamline at SPring-8. The incident beam (wavelength = 0.6887 Å) was focused to 250 μm^2 by a toroidal mirror. The samples were sealed in capillaries (diameter 0.5 mm) under an Ar atmosphere. The diffraction data were analyzed using the Rietveld analysis program RIETAN2000 [11].

Zero-field (ZF)- and longitudinal field (LF)-μSR experiments were performed using the Advanced Research Targeted Experimental Muon Instrument at the S line (ARTEMIS) spectrometer [12] with a fly-past chamber at the Material and Life Science Experimental Facility (MLF), J-PARC, Tokai, Japan.

III. RESULTS AND DISCUSSION

A. Crystal structure

Figure 1 shows the synchrotron x-ray diffraction patterns of $x = 0$ and 0.1. The diffraction patterns of the La-doped samples indicate a tetragonal structure in the $I4_1/acd$ space group. The final reliable factors ranged from 2.04% to 3.01%. In the $x = 0.2$ sample, a small amount of impurity phase (La_2O_3) was observed. The lattice parameters and the Ir-O-Ir bond angles of ball-milled $Sr_{2-x}La_xIrO_4$ are summarized in Fig. 2. The a axis expands with x, while the c axis shrinks. The contracted c axis can be explained by the much smaller ionic radius of La^{3+} (1.216 Å) compared to that of Sr^{2+} (1.31 Å). However, this idea is inconsistent with the expanded a axis. As the a axis reflects the Ir-O bond length in the IrO_2 plane, its enhancement might be due to electron doping in the Ir-O antibonding orbitals. Indeed, the Ir-O-Ir bond angle increases monotonically with La substitution. To clarify the structural differences between ours and previous results, we studied the results of two earlier reports [8,9]. In a polycrystalline sample [8], the doping dependence of the lattice parameters was similar to our observations, but the quantitative values largely differed from our data. On the other hand, the structural parameters of single-crystalline samples [9] explained both the trend and values of the doping dependence. Thus the structural parameters of the MA samples are quantitatively consistent with the single-crystal sample.

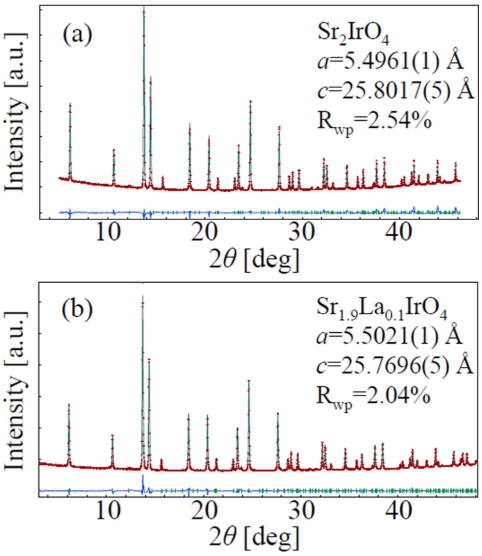

FIG. 1. Synchrotron x-ray diffraction patterns of (a) $x = 0$ and (b) $x = 0.1$. The data were fitted with the $I4_1/acd$ crystal structure model.

From spatially resolved optical second- and third-harmonic generation rotational anisotropy measurements, Torchinsky *et al.* recently reported a decrease in symmetry from $I4_1/acd$ to $I4_1/a$ in Sr_2IrO_4 below T_N [13]. To explore the structural changes below and above T_N (~240 K), we performed synchrotron x-ray measurements from 300 to 100 K. Although we detected no structural changes below T_N, we observed negative thermal expansions [Fig. 2(d)]. According to Ranjbar *et al.* [14], negative thermal expansion of the c axis reflects a structural phase transition from $I4_1/acd$ to $I4/mmm$ near 1123 K. Thus this unusual behavior probably originates from the structural phase transition.

B. Resistivity

Figure 3(a) shows the electrical resistivity ρ of $Sr_{2-x}La_xIrO_4$. All samples ($x = 0$, 0.1, and 0.2) exhibit semiconducting behavior, and ρ at 300 K decreases by two orders of magnitude in the La-doped samples. This behavior agrees with previous reports, including measurements of single crystals [9]. However, the observed results contrast with a previous report discussing the introduction of impurity centers by La doping [8], in which the resistivity increased at 300 K. The decreased resistivity observed here strongly supports that La was successfully doped into $Sr_{2-x}La_xIrO_4$ in the milling technique.

In a previous report of single-crystal Sr_2IrO_4, the resistivity did not display simple Arrhenius-type behavior [$\rho(T) = \rho_0 \exp(\Delta/k_BT)$] [15], but was well fitted by the three-dimensional variable range hopping (VRH) model [$\rho(T) = \rho_0 \exp(\Delta/k_BT)^\nu$] with $\nu = 1/4$ over a certain temperature range. Similar behavior is depicted in Fig. 3(b). The curve of $x = 0$ fits the aforementioned VRH model below 60 K, while that of $x = 0.1$ shows similar behavior over a wider range (below 100 K). The good fits to the VRH model indicate that the behavior of the carriers in these systems is not simply thermally activated. In contrast, the resistivity at $x = 0.2$ displays Arrhenius-type behavior over the entire temperature range. The calculated gap Δ changed to 11.5 meV ($x = 0$), 12.0 meV ($x = 0.1$), and 2.7 meV ($x = 0.2$). The decrease in the energy gap suggests that electron carriers are introduced into the IrO_2 plane via La substitution. This behavior agrees well with the evolved in-gap state induced by La doping, as observed in ARPES measurements of single-crystalline samples [3], as well as the previous resistivity measurement results using single-crystalline samples [9]. The behavior contradicts the previous report on polycrystalline samples, in which the energy gap Δ slightly increased from 47 meV ($x = 0$) to 55 meV ($x = 0.2$) after La doping [8]. Thus

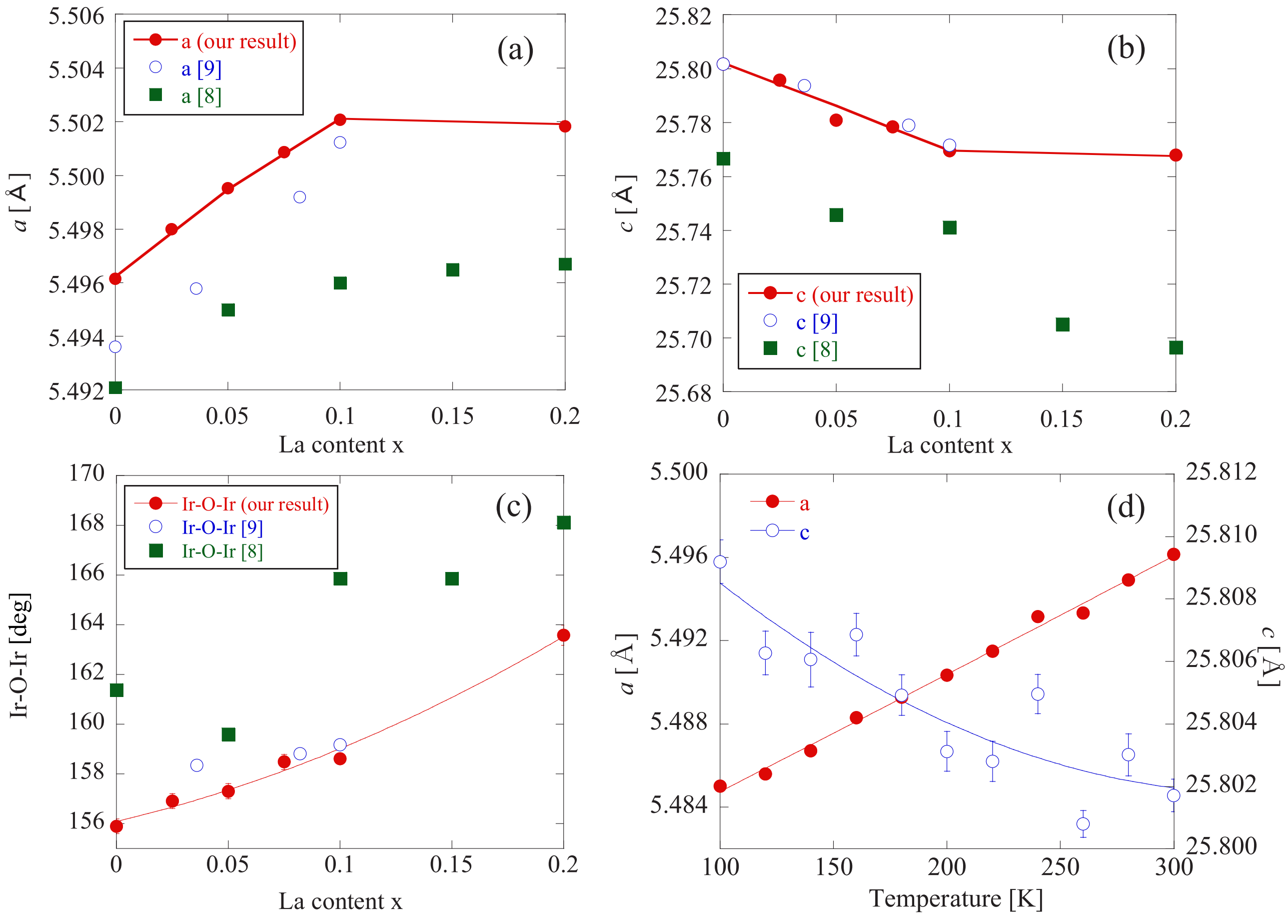

FIG. 2. (a) a-axis and (b) c-axis lattice constants and (c) Ir-O-Ir bond angles of ball-milled $\mathrm{Sr}_{2-x}\mathrm{La}_x\mathrm{IrO}_4$. Structural parameters of a previous polycrystalline sample (closed squares, Ref. [8]) and a single-crystalline sample (open circles, Ref. [9]) are also shown. (d) Temperature dependence of the lattice constants in $\mathrm{Sr}_2\mathrm{IrO}_4$.

the result indicates here that the mechanical milling technique enables us to synthesize the crystals of which the electrical transport is not bound by grain boundaries which have been limiting the studies of the materials in polycrystalline samples. We also note that the La doping was applied over a wider range in our experiment than in single-crystal experiments, and was similar to the doping range of polycrystalline samples.

To examine the effects of mechanical milling on the morphology of polycrystalline $\mathrm{Sr}_{2-x}\mathrm{La}_x\mathrm{IrO}_4$ samples, we characterized these samples by SEM. Figures 4(a) and 4(b) show

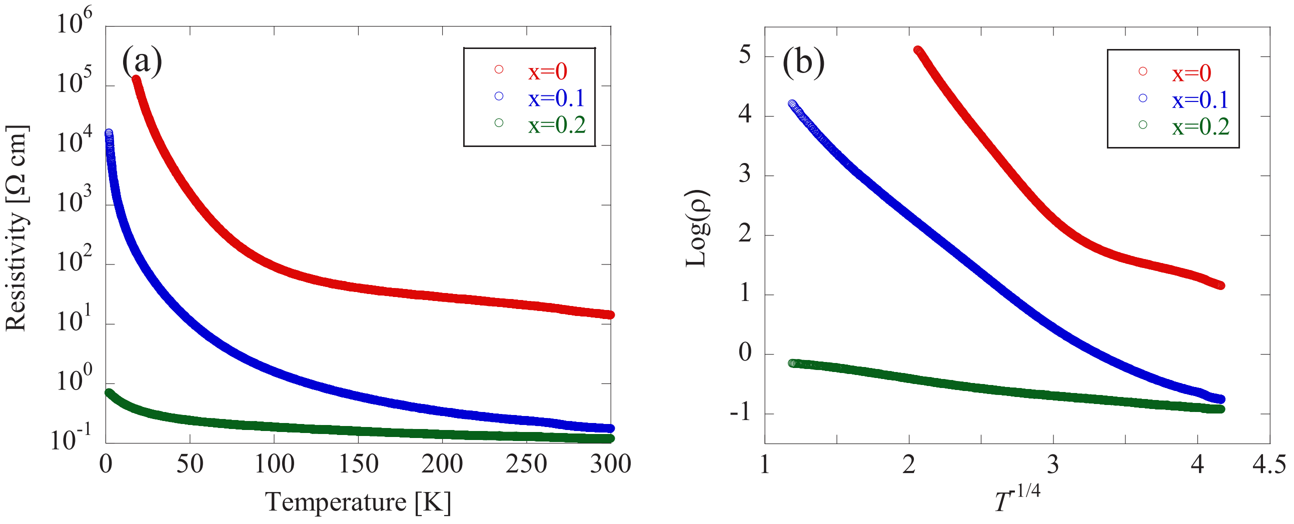

FIG. 3. Temperature dependence of the (a) electrical resistivity in $\mathrm{Sr}_{2-x}\mathrm{La}_x\mathrm{IrO}_4$; (b) $\ln\rho$ vs $T^{-1/4}$ from 2 to 300 K.

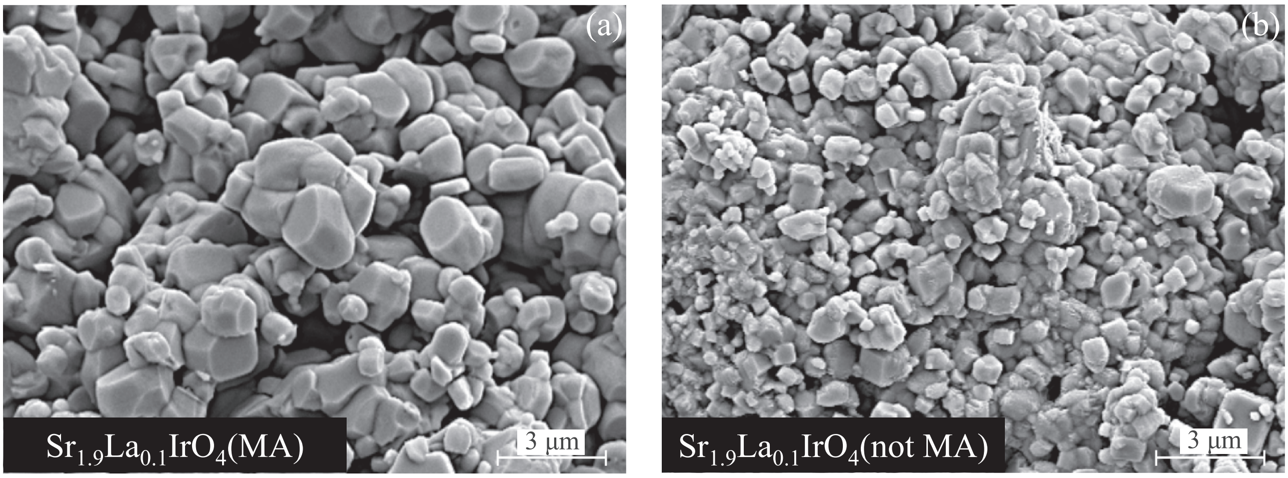

FIG. 4. SEM images of $Sr_{1.9}La_{0.1}IrO_4$: (a) with ball milling, (b) without ball milling.

the surface morphologies of the MA-prepared $Sr_{1.9}La_{0.1}IrO_4$ and the nonalloyed samples, respectively. Comparing the two samples, there are fewer grains in the MA samples at the same scale length, indicating that a post-MA reaction increased the size of the crystal grains and reduced the number of grain boundaries. Therefore, the resistivity difference between our results and those of previous powder studies might originate from grain size and boundary effects.

C. Magnetic susceptibility

Figures 5(a) and 5(b) shows the magnetic susceptibility of $Sr_{2-x}La_xIrO_4$. Note that at low temperature, the magnitude of the saturated magnetic susceptibility decreases with increasing La concentration. La doping has been reported to strongly modulate the Ir-O-Ir bond angles [8,9]; thus the present decrease might originate not only from the carrier doping, but also from the approach of the Ir-O-Ir bond angles toward 180°. Both effects would clearly decrease the T_N. In the present study, T_N monotonically decreased from 240 K ($x = 0$) to 114 K ($x = 0.13$).

The above results imply a strong relationship between the crystal structure and its magnetism. Recently, Jackeli and Khaliullin [16] and Liu *et al.* [17] reported the influences of structural perturbations on spin ordering, in particular on the spin canting angle. They constructed a detailed magnetic phase diagram showing the transition from the canted ground state to different types of collinear magnetic states as a function of the octahedral tetragonal distortion (c/a). These theoretical studies strongly suggest that c/a is coupled to the magnetism of the Sr214 system. To experimentally clarify the relationship between the crystal structure and its magnetism, we plotted T_N against c/a in $Sr_{2-x}La_xIrO_4$. As shown in Fig. 6, T_N decreased with decreasing c/a in this compound. Perkins *et al.* calculated significant changes in the isotropic exchange coupling J due to the tetragonal distortion [18]. They found that increasing the tetragonal distortion increases the exchange coupling J. In this theoretical calculation, the suppression of T_N by c/a can be explained by the decreased exchange coupling of J. Similar T_N vs c/a trends have been observed experimentally in Ca doping [19] and Tb doping [20]. These results suggest that the magnetism of a Sr214 system is strongly correlated with the parameters of its crystal structure, such as c/a.

Figure 7 shows the magnetic phase diagram of $Sr_{2-x}La_xIrO_4$ synthesized by MA and single-crystalline samples [9]. The La dependence of T_N in our results favorably

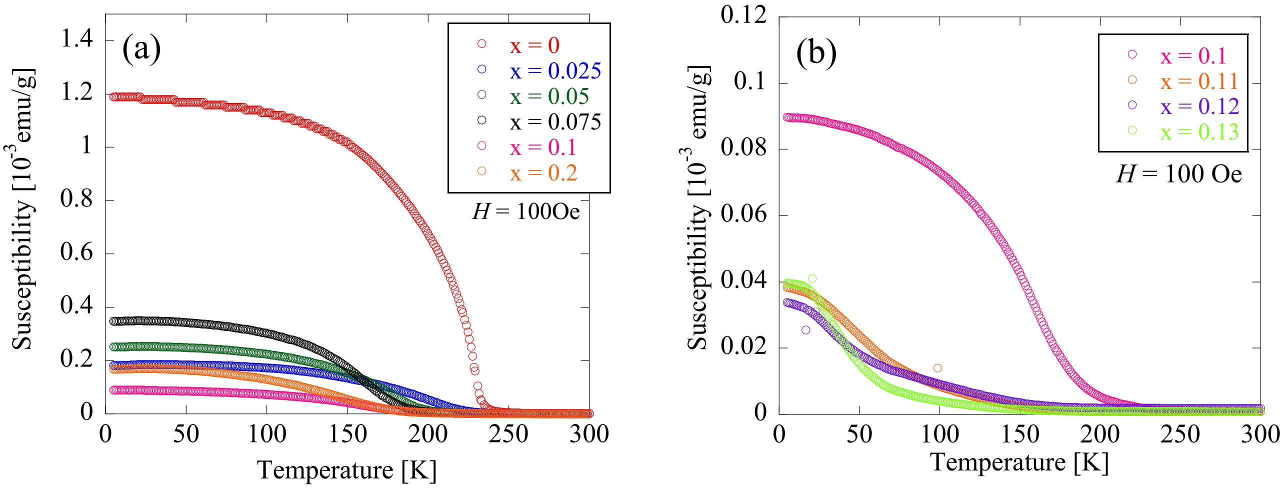

FIG. 5. Temperature dependence of the (a,b) magnetic susceptibility in $Sr_{2-x}La_xIrO_4$.

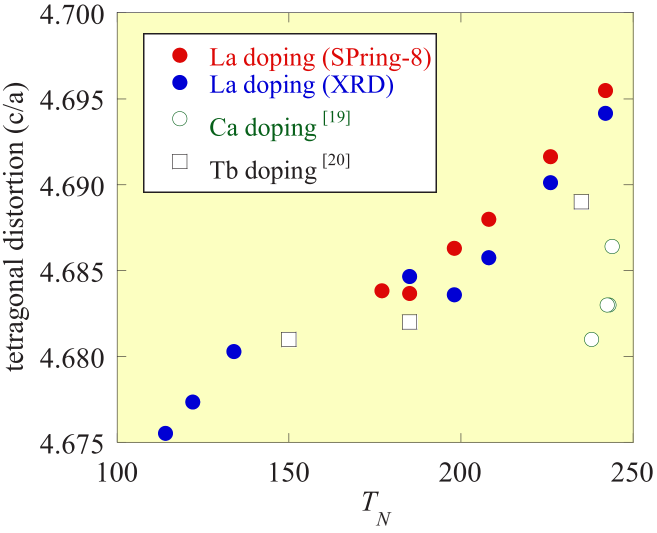

FIG. 6. Relationship between the tetragonal distortion c/a and magnetic transition temperature T_N in Sr214 systems. The Ca- and Tb-doping results were obtained from Refs. [19,20].

agrees with the results of single-crystalline samples. Previous studies reported a short-range AF order above $x = 0.08$ because they found no magnetic Bragg peak measured by neutron scattering. However, it was mentioned that the detection limit of magnetic scattering is $0.06\,\mu_B$ in the Sr214 system. Thus it remains unclear whether a short-range AF above $x = 0.08$ can be observed.

D. μSR measurement

The above uncertainty was clarified in μSR experiments. μSR is one of the most effective techniques for detecting short-range magnetic orders and small magnetic moments with extremely high sensitivity (10^{-2}–$10^{-3}\,\mu_B$) [21]. Figure 8(a) shows selected ZF-μSR time spectra of $Sr_{1.9}La_{0.1}IrO_4$ in the temperature range 3.4–300 K. Nonoscillatory signals are present, indicating the absence of a long-range-magnetic order even below T_N (∼180 K), as also determined by magnetic susceptibility measurements [see Fig. 5(b)]. The oscillations are not completely absent, but the spectral damping becomes faster with decreasing temperature and the spectrum at 3.4 K shows a shallow "dip" that signals freezing of fluctuating random local fields, where the line shape is close to that of a quasistatic spin-glass state [22]. Recently, Chen *et al.* reported a low-temperature cusp in zero-field cooling (ZFC) data and a slight decrease in the transition temperature, T_F, as the La concentration increased. Specifically, T_F reduced from 13 K for $x = 0.02$ to 9 K for $x = 0.12$ [9]. To further probe the transition at T_F, they performed low-temperature ac susceptibility measurements on the $x = 0.02$ sample. They found that the peak of the ZFC shifts to higher temperatures with increasing probe frequency. These results support the existence of a spin-glass state at low temperature in doped $Sr_{2-x}La_xIrO_4$. The time evolution of the spectra above 14 K can be fitted by the following function:

$$A_{ZF}(t) = A_s \exp(-\lambda t)^{\beta} + A_{bg}. \tag{1}$$

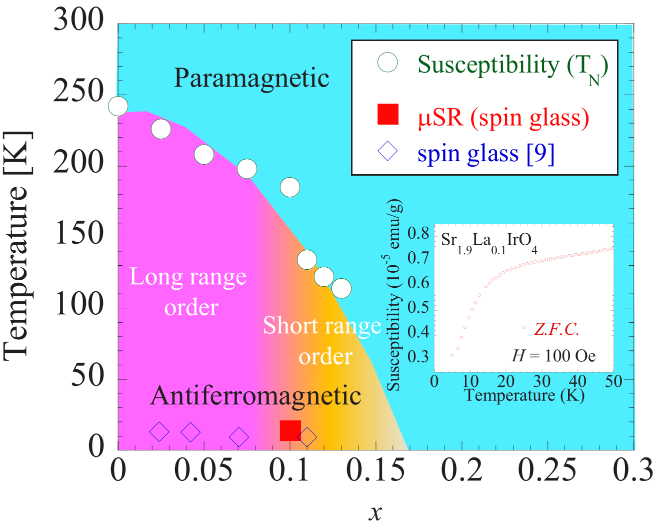

FIG. 7. Magnetic phase diagram of $Sr_{2-x}La_xIrO_4$ determined from magnetic susceptibility and μSR measurements. Inset shows the magnetic susceptibility data ($x = 0.1$) under a zero-field cooling process.

Here, A_s and A_{bg} are the positron decay asymmetries (amplitudes) of the sample ($A_s = 0.2048$) and background ($A_{bg} = 0.0293$, mainly from a silver plate) components, respectively; λ is the relaxation rate; and β is the stretching exponent. Note that the spectra below 300 K are not easily fitted by a simple exponential function ($\beta = 1$). In μSR analyses, the stretched exponential function is often used to phenomenologically describe relaxation in disordered systems in which the distribution of the relaxation time broadens. The fitting may deteriorate below 14 K due to mixing of the low-temperature phase, as described later.

Figure 8(b) shows the temperature dependences of λ and β. A three-step decrease appears in β as the temperature decreases. As evidenced in the lower panel of Fig. 8(b), β begins to decrease from approximately 300 K, suggesting the development of short-range spin correlations between the intralayer Ir ions. Subsequently, a gradual decrease of β from 0.8 to 0.6 appears around 180 K, corresponding to T_N. Because this behavior is often observed in frustrated antiferromagnets, the magnetic state below T_N was determined as a short-range AF order coexisting with spin fluctuation that is detectable within the muon time scale. This situation can also be explained as a Griffiths phase, in which short-range AF clusters occur and grow upon cooling in the paramagnetic phase. Spin autocorrelation functions in the Griffiths phase can be described by a stretched exponential of the form $\exp(-\lambda t)^{\beta}$ with $\beta = 0.5$ [23], which is also consistent with our fitting results. In fact, an electronic inhomogeneity has been observed in scanning tunneling microscopy (STM) measurements [9], which is attributed to inhomogeneous carrier distribution. Thus these inhomogeneous spin dynamics may be naturally associated with the intermixing of different magnetic phases such as the Griffiths phase.

As the temperature decreases further (to below 50 K), β reaches around 1/3, a typical value in dilute spin-glass systems [24,25]. The relaxation rate λ also increases rapidly in this

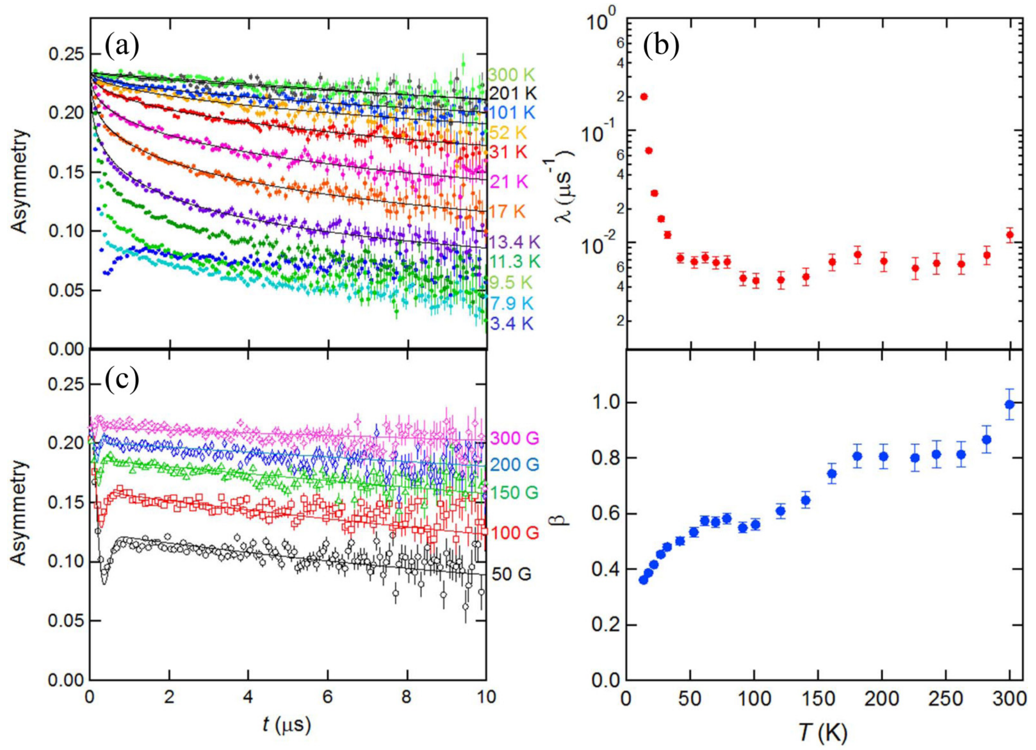

FIG. 8. (a) Temperature dependence of ZF-μSR time spectra for $\mathrm{Sr_{1.9}La_{0.1}IrO_4}$. Solid lines represent the fitting results using Eq. (1). (b) Temperature dependence of the relaxation rate λ and the stretching exponent β. (c) LF-μSR time spectra at 3.4 K. Solid lines represent the best fit results using Eq. (4).

temperature region [see upper panel of Fig. 8(b)]. This implies a critical slowdown of the spin fluctuation toward a spin-glass transition. Indeed, our magnetic susceptibility data ($x = 0.1$) under the ZFC process show a kink at 15 K. As similar behaviors have been reported in previous studies [9], we conclude that $\mathrm{Sr_{1.9}La_{0.1}IrO_4}$ has a magnetic phase transition between the short-range order and the spin-glass state at around 14 K.

To more clearly distinguish the low-temperature spin-glass state, we performed LF-μSR measurements on $\mathrm{Sr_{1.9}La_{0.1}IrO_4}$. By applying an external magnetic field parallel to the initial direction of muon-spin polarization, one can evaluate the size of the static-random field at the muon stopping site in a material. Figure 8(c) shows the LF-μSR time spectra of $\mathrm{Sr_{1.9}La_{0.1}IrO_4}$ at 3.4 K under several LFs (50, 100, 150, 200, and 300 G). As the LF increases, the persisting asymmetry is enhanced under restoration of the initial muon polarization; this is usually called the decoupling effect. The decoupling behavior in Fig. 8(c) clearly indicates that most of the Ir electronic spins are static in this state. When the electronic spins are static, dense, and randomly oriented, the LF muon polarization function for a Gaussian local field becomes

$$G_z^{KT}(t,H_L) = 1 - \left(\frac{2\Delta^2}{\omega_L^2}\right)\left[1 - \exp\left(\frac{-\Delta^2 t^2}{2}\right)\cos(\omega_L t)\right] + \left(\frac{2\Delta^4}{\omega_L^3}\right)\int_0^t \exp\left(\frac{-\Delta^2 t^2}{2}\right)\sin(\omega_L \tau)d\tau, \quad (2)$$

where Δ is proportional to the root-mean square of the local field distribution (Gaussian linewidth), H_L is the longitudinal field, and $\omega_L = \gamma_\mu H_L$ (γ_μ: muon gyromagnetic ratio = $2\pi \times$ 135.54 MHz/T). Here, we further investigate the contribution of the spin fluctuation ν as the influence from the neighboring short-range ordered phase. Based on the strong collision model [26,27], the muon-spin polarization function is given as

$$G_z^{KT}(t,H_L,\nu) = G_z^{KT}(t,H_L)\exp(-\nu t) + \nu\int_0^t \exp(-\nu t) \times G_z^{KT}(t,H_L)G_z^{KT}(t-\tau,H_L,\nu)d\tau. \quad (3)$$

Replacing the first term on the right side of Eq. (1) with this form, we obtain

$$A_{\mathrm{LF}}(t,H_L) = A_s G_z^{KT}(t,H_L,\nu) + A_{\mathrm{bg}}. \quad (4)$$

The curves are well fitted by the above function, as shown in Fig. 8(c), by sharing the field-independent parameters, A_s, A_{bg}, Δ, and ν, the so-called global fit. The parameters were extracted as $\Delta = 4.47(3)\mu s^{-1}$ and $\nu = 0.111(3)$ MHz; thus the characteristic field at a muon site was determined as $\Delta/\gamma_\mu =$ 52.5(3)G, approximately two orders of magnitude larger than that of the nuclear magnetic moment (~0.3 G) [28].

Before discussing the Ir moment size, we should determine where the implanted muon is located in $\mathrm{Sr_{1.9}La_{0.1}IrO_4}$. The previous μSR study [29] stated that there are two main types of muon sites in $\mathrm{Sr_2IrO_4}$; one near the apical oxygen, the other near the in-plane oxygen. However, the implanted muons do not occupy these sites equally: more than 90% of the muons are located in the apical oxygen site ($\theta = 60°$, $\phi = 45°$, $r = 1$ Å from the apical oxygen) of $\mathrm{Sr_2IrO_4}$. We thus assume that all implanted muons occupy the apical oxygen site in

$Sr_{1.9}La_{0.1}IrO_4$ (as in Sr_2IrO_4), because both crystal structures ($x = 0$ and $x = 0.1$) are nearly unchanged.

We now estimate the Ir moment size of $Sr_{1.9}La_{0.1}IrO_4$. In Sr_2IrO_4, the moment size of the $J_{\rm eff} = 1/2$ pseudospin is reduced to $\sim 0.4\,\mu_{\rm B}$, as confirmed by previous μSR, RIXS, and neutron diffraction measurements [9,29,30]. Although a pseudospin of $J_{\rm eff} = 1/2$ is almost equivalent to the superposition of a magnetic dipole and an octopole, the local field $B_{\rm loc}$ at the muon site is given by the vector summation of the pointlike magnetic dipoles situated at the Ir sites, because the octopole makes a relatively small contribution to reducing the total magnetic induction. Note that the transferred moment from Ir to O is negligibly small (a few percent of $0.4\,\mu_{\rm B}$) in Sr_2IrO_4 [29]. The Gaussian linewidth Δ is given as the dipole summation,

$$\Delta = \left[\frac{2}{3}\gamma_\mu^2 \sum_j \langle |\hat{A}_j \mu_j| \rangle^2\right]^{1/2}, \tag{5}$$

for possible muon sites, where $\hat{A}_j$ is the dipole tensor expressed as

$$\hat{A}_j = \frac{1}{r_j^3}\left(\frac{3\alpha_i\beta_j}{r_j^2} - \delta_{\alpha\beta}\right) \ (\alpha,\beta = x,y,z). \tag{6}$$

The summation runs through the jth Ir moments μ_j located at $r_{\rm j} = (x_{\rm j}, y_{\rm j}, z_{\rm j})$ from a given muon site. The local field $B_{\rm loc}$ at the muon site is given by

$$B_{\rm loc} = \left|\sum_j \hat{A}_j \mu_j\right|. \tag{7}$$

Therefore, the root-mean-square value of the local field $\langle B_{\rm loc}\rangle_{\rm rms}$ is proportional to the Gaussian linewidth Δ. Each muon will experience magnetic fields from the local fields that obey the same Gaussian distribution.

As noted earlier, the analysis of the LF-μSR data yielded $\Delta = 4.47(3)\,\mu{\rm s}^{-1}$ for $Sr_{1.9}La_{0.1}IrO_4$. By substituting this value into Eq. (5) and calculating the dipolar summation using the DIPELEC205 code [28], the effective Ir moment size $|\mu_{\rm Ir}|$ was determined as $0.0452(3)\,\mu_{\rm B}$. This value is about one-tenth that of Sr_2IrO_4 ($0.4\,\mu_{\rm B}$) [9,29,30], so the decrease of the Ir moment is attributed to the effects of electron doping by La substitution. Incidentally, the spontaneous magnetization in the short-range ordered phase also reduces the value to less than one-tenth in the $x = 0.1$ sample [see Fig. 5(a)]. This suggests that the Ir moment is reduced even in the short-range ordered phase, consistent with the fact that such a small ordered moment ($0.045\,\mu_{\rm B}$) is difficult to resolve in neutron diffraction.

Although we have clarified the short-range magnetic order in $Sr_{1.9}La_{0.1}IrO_4$, how the long-range order changes to a short-range order with electron doping in the Sr214 system remains unclear. To clarify the magnetic phase diagram in the Sr214 system, we will perform μSR experiments in electron-doped $Sr_{2-x}La_xIrO_4$ [$x = 0.05$ ($T_{\rm N} \sim 208$ K), $x = 0.075$ ($T_{\rm N} \sim 198$ K), and $x = 0.13$ ($T_{\rm N} \sim 114$ K)] in future work.

ACKNOWLEDGMENTS

We would like to acknowledge K. Kawashima, S. Suzuki, and S. Yasuda for collaboration in the early stage of the experiment. We also would like to acknowledge M. Nagao and A. Miura for valuable discussion. The authors are grateful to K. Tomimoto at the Center for Instrumental Analysis for the scanning electron microscope measurements. The muon experiment at the Materials and Life Science Experimental Facility of the J-PARC was performed under a user program (Proposal No. 2018A0254). This work was supported by Grants-in-Aid from the Ministry of Education, Culture, Sports, Science and Technology (MEXT) under Grants No. 2500003, No. 26247057, No. 16K17750, and No. 2704, and was partially supported by the Electric Power Development Company Limited (Dengenkaihatsu) and Program for Advancing Strategic International Networks to Accelerate for Circulation of Talented Researchers from the Japan Society for the Promotion of Science (R2705).

---

[1] B. J. Kim, H. Jin, S. J. Moon, J.-Y. Kim, B.-G. Park, C. S. Leem, J. Yu, T. W. Noh, C. Kim, S.-J. Oh, J.-H. Park, V. Durairaj, G. Cao, and E. Rotenberg, Phys. Rev. Lett. **101**, 076402 (2008).

[2] J. Kim, D. Casa, M. H. Upton, T. Gog, Y.-J. Kim, J. F. Mitchell, M. van Veenendaal, M. Daghofer, J. van den Brink, G. Khaliullin, and B. J. Kim, Phys. Rev. Lett. **108**, 177003 (2012).

[3] K. Terashima, M. Sunagawa, H. Fujiwara, T. Fukura, M. Fujii, K. Okada, K. Horigane, K. Kobayashi, R. Horie, J. Akimitsu, E. Golias, D. Marchenko, A. Varykhalov, N. L. Saini, T. Wakita, Y. Muraoka, and T. Yokoya, Phys. Rev. B **96**, 041106(R) (2017).

[4] A. Ino, C. Kim, M. Nakamura, T. Yoshida, T. Mizokawa, Z.-X. Shen, A. Fujimori, T. Kakeshita, H. Eisaki, and S. Uchida, Phys. Rev. B **62**, 4137 (2000).

[5] N. P. Armitage, F. Ronning, D. H. Lu, C. Kim, A. Damascelli, K. M. Shen, D. L. Feng, H. Eisaki, Z.-X. Shen, P. K. Mang, N. Kaneko, M. Greven, Y. Onose, Y. Taguchi, and Y. Tokura, Phys. Rev. Lett. **88**, 257001 (2002).

[6] H. Watanabe, T. Shirakawa, and S. Yunoki, Phys. Rev. Lett. **110**, 027002 (2013).

[7] Z. Y. Meng, Y. B. Kim, and H. Y. Kee, Phys. Rev. Lett. **113**, 177003 (2014).

[8] C. Cosio-Castaneda, C. Tavizon, A. Baeza, P. de la Mora, and R. Escudero, J. Phys.: Condens. Matter **19**, 446210 (2007).

[9] X. Chen, T. Hogan, D. Walkup, W. Zhou, M. Pokharel, M. Yao, W. Tian, T. Z. Ward, Y. Zhao, D. Parshall, C. Opeil, J. W. Lynn, V. Madhavan, and S. D. Wilson, Phys. Rev. B **92**, 075125 (2015).

[10] T. F. Qi, O. B. Korneta, S. Chikara, M. Ge, S. Parkin, L. E. De Long, P. Schlottmann, and G. Cao, J. Appl. Phys. **109**, 07D906 (2011).

[11] F. Izumi and T. Ikeda, Mater. Sci. Forum **321–324**, 198 (2000).

[12] K. M. Kojima, T. Murakami, Y. Takahashi, H. Lee, S. Y. Suzuki, A. Koda, I. Yamauchi, M. Miyazaki, M. Hiraishi, H. Okabe, S. Takeshita, R. Kadono, T. Ito, W. Higemoto, S. Kanda, Y. Fukao, N. Saito, M. Saito, M. Ikeno, T. Uchida, and M. M. Tanaka, J. Phys. Conf. Ser. **551**, 012063 (2014).

[13] D. H. Torchinsky, H. Chu, L. Zhao, N. B. Perkins, Y. Sizyuk, T. Qi, G. Cao, and D. Hsieh, Phys. Rev. Lett. **114**, 096404 (2015).

[14] B. Ranjbar and B. J. Kennedy, J. Solid State Chem. **232**, 178 (2015).

[15] G. Cao, J. Bolivar, S. McCall, J. E. Crow, and R. P. Guertin, Phys. Rev. B **57**, R11039 (1998).
[16] G. Jackeli and G. Khaliullin, Phys. Rev. Lett. **102**, 017205 (2009).
[17] P. Liu, S. Khmelevskyi, B. Kim, M. Marsman, D. Li, X.-Q. Chen, D. D. Sarma, G. Kresse, and C. Franchini, Phys. Rev. B **92**, 054428 (2015).
[18] N. B. Perkins, Y. Sizyuk, and P. Wölfle, Phys. Rev. B **89**, 035143 (2014).
[19] G. Zhou, X. Gu, X. Yang, X. Gao, K. Wang, J. Peng, F. Zhang, and X. S. Wu, AIP Adv. **7**, 055823 (2017).
[20] J. C. Wang, S. Aswartham, F. Ye, J. Terzic, H. Zheng, D. Haskel, S. Chikara, Y. Choi, P. Schlottmann, R. Custelcean, S. J. Yuan, and G. Cao, Phys. Rev. B **92**, 214411 (2015).
[21] A. Amato, Rev. Mod. Phys. **69**, 1119 (1997).
[22] Y. J. Uemura, T. Yamazaki, D. R. Harshman, M. Senda, and E. J. Ansaldo, Phys. Rev. B **31**, 546 (1985).
[23] A. J. Bray, Phys. Rev. Lett. **59**, 586 (1987).
[24] I. A. Campbell, A. Amato, F. N. Gygax, D. Herlach, A. Schenck, R. Cywinski, and S. H. Kilcoyne, Phys. Rev. Lett. **72**, 1291 (1994).
[25] A. Keren, P. Mendels, I. A. Campbell, and J. Lord, Phys. Rev. Lett. **77**, 1386 (1996).
[26] R. S. Hayano, Y. J. Uemura, J. Imazato, N. Nishida, T. Yamazaki, and R. Kubo, Phys. Rev. B **20**, 850 (1979).
[27] K. W. Kehr, G. Honig, and D. Richter, Z. Phys. B **32**, 49 (1978).
[28] The dipolar fields calculated by DIPELEC205 code; K. M. Kojima, J. Yamanobe, H. Eisaki, S. Uchida, Y. Fudamoto, I. M. Gat, M. I. Larkin, A. Savici, Y. J. Uemura, P. P. Kyriakou, M. T. Rovers, and G. M. Luke, Phys. Rev. B **70**, 094402 (2004).
[29] M. Miyazaki, R. Kadono, M. Hiraishi, A. Koda, K. M. Kojima, K. Ohashi, T. Takayama, and H. Takagi, Phys. Rev. B **91**, 155113 (2015).
[30] C. Dhital, T. Hogan, Z. Yamani, C. de la Cruz, X. Chen, S. Khadka, Z. Ren, and S. D. Wilson, Phys. Rev. B **87**, 144405 (2013).